Bilayered VOPO$_4$·2H$_2$O Nanosheets with High-Concentration Oxygen Vacancies for High-Performance Aqueous Zinc-Ion Batteries

Zeyi Wu, Chengjie Lu, Fei Ye, Lin Zhang, Le Jiang, Qiang Liu, Hongliang Dong, Zhengming Sun, and Linfeng Hu*

2D materials with atomically precise thickness and tunable chemical composition hold promise for potential applications in nanoenergy. Herein, a bilayer-structured VOPO$_4$·2H$_2$O (bilayer-VOP) nanosheet is developed with high-concentration oxygen vacancies ([Vö]) via a facile liquid-exfoliation strategy. Galvanostatic intermittent titration technique study indicates a 6 orders of magnitude higher zinc-ion coefficient in bilayer-VOP nanosheets (4.6 × 10^{-7} cm^{-2} s^{-1}) compared to the bulk counterpart. Assistant density functional theory (DFT) simulation indicates a remarkably enhanced electron conductivity with a reduced bandgap of ≈0.2 eV (bulk sample: 1.5 eV) along with an ultralow diffusion barrier of ≈0.08 eV (bulk sample: 0.13 eV) in bilayer-VOP nanosheets, thus leading to superior diffusion kinetics and electrochemical performance. Mott–Schottky (impedance potential) measurement also demonstrates a great increase in electronic conductivity with ≈57-fold increased carrier concentration owing to its high concentration [Vö]. Benefited by these unique features, the rechargeable zinc-ion battery composed of bilayer-VOP nanosheets cathode exhibits a remarkable capacity of 313.6 mAh g^{-1} (0.1 A g^{-1}), an energy density of 301.4 Wh kg^{-1}, and a prominent rate capability (168.7 mAh g^{-1} at 10 A g^{-1}).

1. Introduction

Layered materials, based on the layered crystallographic structure and liquid-exfoliation behavior, have been particularly studied in rechargeable battery application for their unique intercalation mechanism.[1,2] Especially, layered hydrated vanadyl phosphate

Z. Y. Wu, L. Zhang, L. Jiang, L. F. Hu
Department of Materials Science
Fudan University
Shanghai 200433, P. R. China
C. J. Lu, F. Ye, Q. Liu, Z. M. Sun, L. F. Hu
School of Materials Science and Engineering
Southeast University
Nanjing 211189, P. R. China
E-mail: linfenghu@seu.edu.cn
H. L. Dong
Center for High Pressure Science and Technology Advanced Research
Shanghai 201203, P. R. China

(VOPO$_4$·2H$_2$O) with the characteristic of corner-shared [VO$_6$] octahedra orderly linked with PO$_4$ tetrahedra as a host layer[3] has been reported as very promising cathode material for ZIBs. The most intriguing feature of layered VOPO$_4$·2H$_2$O should be attributed to its high discharge plateau (≈1.1–1.2 V vs Zn^{2+}/Zn) benefitting by the "inductive effect" originated from the strong P—O covalent bonds inside its in-plane structure remarkably enhances the iconicity of the V—O bonds,[3,4] and thus in favor of the higher energy density compared to other V-based oxides and derivatives. In addition, the expansive 2D interlayer spacing (≈7.4 Å) is also in support of the facile transport channel for fast zinc-ion diffusion.[5,6] Previous study demonstrates that VOPO$_4$·2H$_2$O is very interesting and promising cathode materials for various metal-ion batteries, including sodium-ion batteries (SIBs), potassium-ion batteries (PIBs), magnesium ion battery (MIBs), calcium-ion battery (CIBs), and aluminum-ion batteries (AIBs).[7]
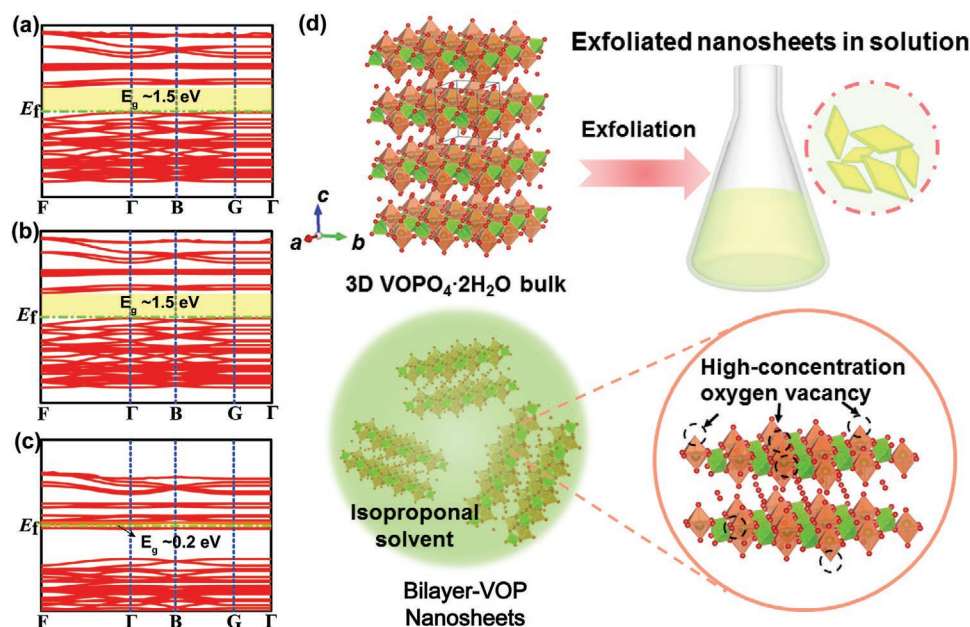
The most recent progress also reveals layered VOPO$_4$·2H$_2$O can be considered as a promising cathode candidate for aqueous rechargeable zinc-ion batteries (ZIBs) owing to its high discharge plateau originated from the aforementioned inductive effect.[8,9] The first development of layered VOPO$_4$·2H$_2$O used in ZIBs cathode was reported by Wang et al. in 2018, who revealed the zinc-ion storage mechanism of layered VOPO$_4$·2H$_2$O framework and simultaneously study the influence of water content in the ZIBs system on the zinc-ion diffusion ability.[10] After this, Chen and co-workers developed a high concentration water-in-salt electrolyte to restrict the O$_2$ evolution and active the oxygen redox process in a high voltage range (>1.8 V), leading to an increased capacity property and higher voltage plateau of the cathode.[5] Sun and co-workers have designed a H$_3$PO$_4$ contained aqueous electrolyte (13 M ZnCl$_2$/0.8 M H$_3$PO$_4$) to inhibit the decomposition and dissolution reaction of VOPO$_4$·2H$_2$O cathode in aqueous electrolyte and promote the voltage and capacity stabilities.[6]

In spite of the high discharge plateau nature of VOPO$_4$·2H$_2$O, the energy density of VOPO$_4$·2H$_2$O-based ZIBs is still significantly limited by its excessively low specific capacity.

**ADVANCED
SCIENCE NEWS**
www.advancedsciencenews.com

**ADVANCED
FUNCTIONAL
MATERIALS**
www.afm-journal.de

Scheme 1. a–c) Calculated band structure diagram of bulk VOPO₄·2H₂O, VOPO₄·2H₂O single atomic layers and [Vö]-rich single atomic layers, respectively. d) Schematic of liquid-phase exfoliation and predictable oxygen vacancy formation in bilayer-VOP nanosheets.

Considering the various valence change of V in VOPO$_4$ framework during the electrochemical reaction, the theoretical specific capacity of layered VOPO$_4$·2H$_2$O should be higher than 300 mAh g^{-1}.[11,12] Nevertheless, up to date, the reported optimal capacity of VOPO$_4$·2H$_2$O cathode in aqueous ZIBs is less than 170 mAh g^{-1}. The main reason should be attributed to the sluggish diffusion of Zn^{2+} and strong electrostatic interactions between Zn^{2+} and VOPO$_4$·2H$_2$O host.[6]

In general, introduction of vacancy generally regulates the electrochemical properties by energy band modification and increase of electrochemical active sites.[13] To reveal the case in layered VOPO$_4$·2H$_2$O, we utilize density functional theory (DFT) calculations to explore the change of band structure after [Vö] introduction. As shown in **Scheme 1**a,b and Figure S1 in the Supporting Information, both VOPO$_4$·2H$_2$O bulk and single-layer atomic crystals exhibit a similar bandgap (E_g) of 1.5 eV, suggesting the decreased thickness of VOPO$_4$·2H$_2$O crystal has no remarkable influences on the electronic conductivities. Interestingly, such a case is quite different with the presence of [Vö], and a much smaller E_g of 0.2 eV has been detected, while the resulted V$_d$ orbit energy drops below the Fermi level and is served as the top of valence band with effective electron filling at 0 K (Scheme 1c). Accordingly, we consider this considerable change on energy band structure should be favorable for the zinc-ion transport. Unfortunately, it remains a challenge to realize high-concentration [Vö] in layered VOPO$_4$·2H$_2$O.

In this work, we found a liquid-exfoliation strategy in isopropanol can introduce a large number of [Vö], producing a high-yield oxygen-vacancy rich, bilayered nanosheets (noted as bilayer-VOP nanosheets, Scheme 1d). Galvanostatic intermittent titration technique (GITT) measurement confirm almost 6 orders of magnitude higher zinc-ion coefficient of the [Vö]-rich bilayer-VOP nanosheets (4.6 × 10^{-7} cm^{-2} s^{-1})

compared with the [Vö]-poor VOPO$_4$·2H$_2$O bulk sample. DFT simulation also shows an extremely low diffusion barrier of ≈0.08 eV for optimized Zn^{2+} transport in such a 2D nanosheets cathode, thus leading to ultrafast diffusion kinetics and superior electrochemical performance. The ZIBs composed of the bilayer-VOP nanosheets exhibits a greatly enhanced capacity of 313.6 mAh g^{-1} (at 0.1 A g^{-1}), an intrinsic high discharge plateau of 1.1 V, and prominent rate capability (168.7 mAh g^{-1} at 10 A g^{-1}), conferring practical applicability for next-generation energy storage systems to address the safety and cost issues toward commercial lithium-ion secondary batteries.

2. Results

2.1. Oxygen Vacancy in Bilayer-VOP Nanosheets

Bright-yellow VOPO$_4$·2H$_2$O powder (bulk-VOPO$_4$) with rectangular plate-like morphology (length: ≈20 μm, width: ≈10 μm) was synthesized via a modified oil-bath refluxing method as-reported in the previous work[3,14] (Figure S2, Supporting Information). We compared the exfoliation behavior of the bulk-VOPO$_4$ when in contact with various solvents including deionized (DI) water, ethanol, acetone, and formamide. After continuous stirring for 24 h, we found bulk-VOPO$_4$ generally dissolved/decomposed in DI water. Colloidal suspensions were also not obtained for these samples in ethanol, acetone, and formamide, and the mixtures remained turbid (**Figure 1**a). Only in isopropanol solvent can we obtain a high-quality colloidal suspension (concentration: 10 mg mL^{-1}) with a typical Tydall effect (Figure 1b,c), suggesting the possible exfoliation of VOPO$_4$·2H$_2$O 3D crystal. Transmission electron microscopy (TEM) observations of this colloidal suspension also confirms typical 2D nanosheet morphology with
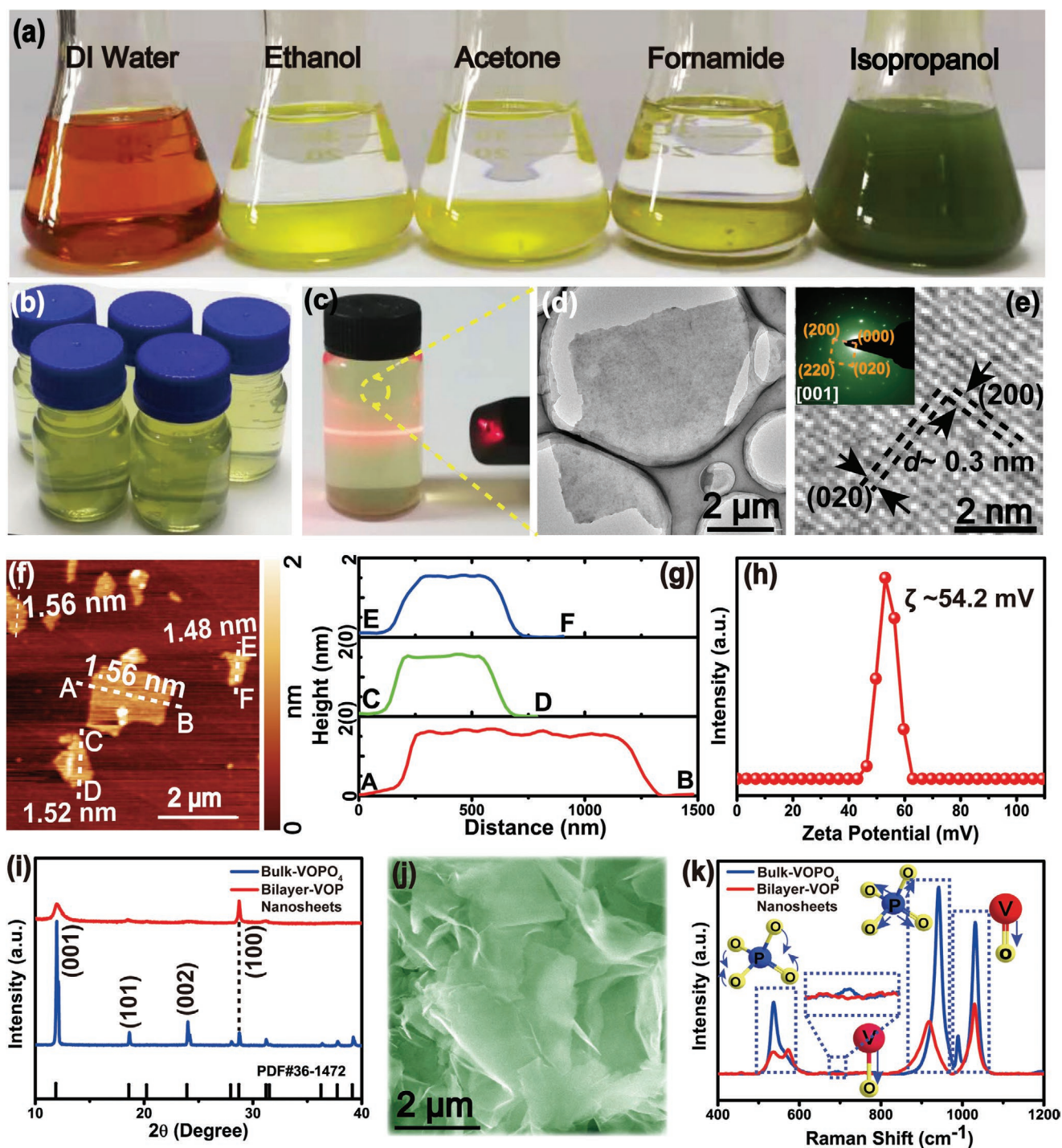
Figure 1. a) Photograph of the colloidal nanosheet suspension from the Bulk-VOPO$_4$ sample in isopropanol and the turbid dispersion in DI water, ethanol, acetone, and formamide after long-term ultrasonic treatment. b) Large-scaled preparation of the bilayer bilayer-VOP nanosheets colloidal suspension with a maximal concentration of 10 mg mL^{-1}. c) Tyndall effect of the colloidal suspension. d) TEM and e) HRTEM image of an individual bilayer nanosheet. Insert is the corresponding SAED pattern. g) AFM image and g) three typical height curves of the nanosheets. h) Zeta-potential distribution curve of the colloidal suspension. i) XRD pattern of bulk-VOPO$_4$ and dried bilayer-VOP nanosheets powders, respectively. j) SEM image. k) Raman spectrum.

a lateral size of several micrometers (Figure 1d). The corresponding high-resolution transmission electron microscopy (HRTEM) taken from the individual nanosheet exhibits clear lattice fringes indexed to (200) and (020) planes, respectively.

Cubic-arranged sharp diffraction spots were observed in the corresponding selected area electron diffraction (SAED) patterns with [001] zone axis, demonstrating the single crystal nature can be well maintained during the liquid-exfoliation

procedure (Figure 1e). Atomic force microscope (AFM) image further demonstrates its thickness of ≈1.5 nm with rather atomically smooth surface. According to the theoretical thickness (≈0.7 nm) of $VOPO_4 \cdot 2H_2O$ monolayer reported in the previous work,[3] the as-observed thickness in our work should be consistent with a bilayer model of layered $VOPO_4 \cdot 2H_2O$ (Figure 1f,g). Given by the Zeta potential test, the nanosheet suspension delivers an average potential of ≈54.2 mV, revealing their positive charge of the exposed nanosheet surface (Figure 1h). Figure 1i shows the X-ray diffraction (XRD) patterns of the bulk-$VOPO_4$ (JCPDS: 84–0111) and the bilayer-VOP nanosheets sample after liquid-exfoliation, respectively. It is evident that the as-exfoliated bilayer-VOP nanosheets sample shows a much lower diffraction intensity compared to their bulk counterpart, indicating the decrease in crystallinity during the swelling/exfoliation process and also usually observed in other liquid-exfoliation treatment. Corresponding scanning electron microscope (SEM) image of further implies its ultrathin morphology as shown in Figure 1j. More importantly, Raman spectrum (Figure 1k) suggests possible [Vo¨] formation for the bilayer nanosheets. The featured band located at around 550, 940, and 1040 cm^{-1} is assigned to δ(O-P-O), ν(O-P), and ν(V=O) mode, respectively.[15,16] With the breaking of hydrogen bonds between the interlayer H_2O and O in $[PO_4]$, O-P stretching shifts to a lower energy due to the mitigatory steric hindrance.[3] Meanwhile, the featured peak of ν(V-O) mode located at ≈700 cm^{-1} dramatically decreases to a very low intensity, implying the possible [Vo¨] formation in $[VO_6]$ octahedra with a weaken ν(V-O) mode.[3,17] Such a result is consistent with the lower crystallinity from the XRD characterization and also agrees well with the electron paramagnetic resonance (EPR) and O 1s X-ray photoelectron spectroscopy (XPS) spectrum as discussed below.

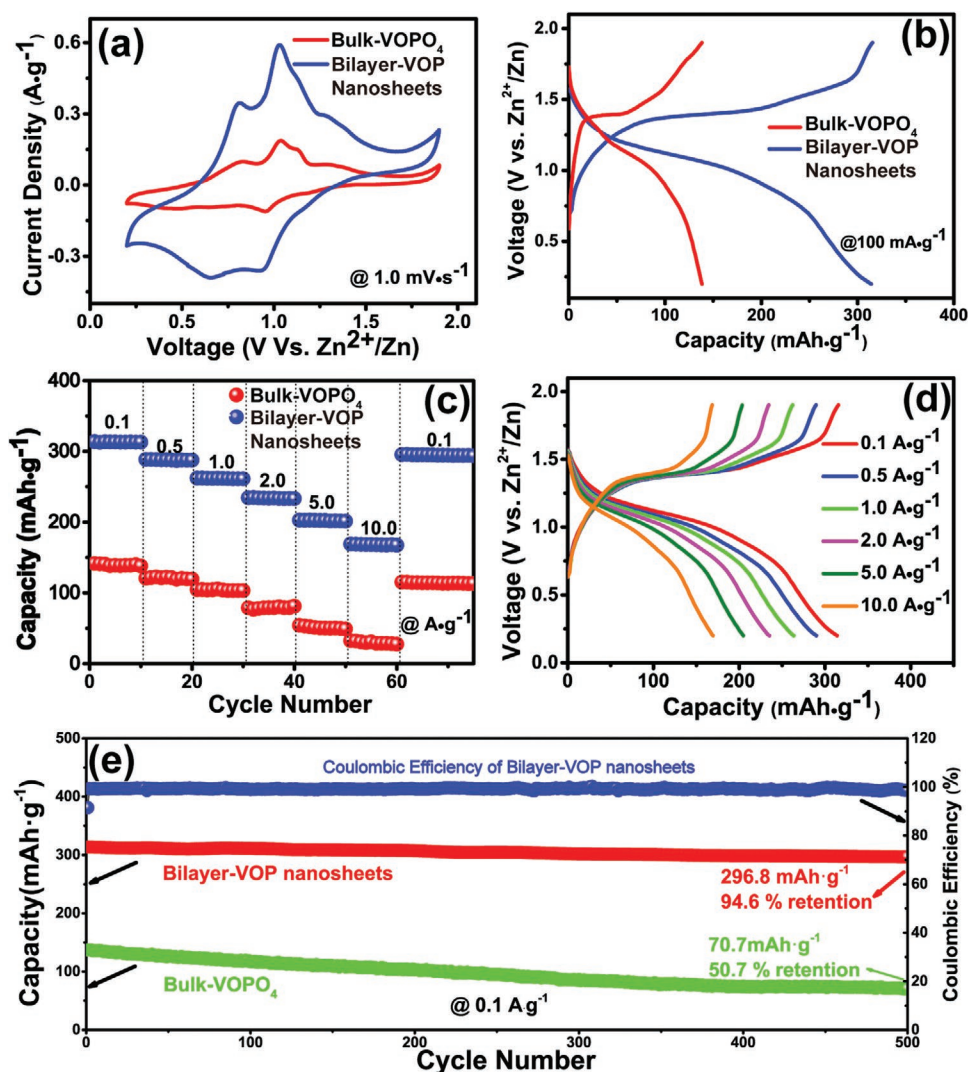## 2.2. Great Enhancement of ZIB Performance

CR-2032 coin cells were assembled employing the bulk-$VOPO_4$ and bilayer-VOP nanosheets as cathode of aqueous ZIBs, respectively. In short, zinc foil and 2 м $ZnSO_4$ aqueous solution was used as anode (counter electrode) and electrolyte, respectively. $Zn/ZnSO_4$/bulk-$VOPO_4$ and $Zn/ZnSO_4$/bilayer-VOP nanosheets cells show the similar cyclic voltammetry (CV) curves at 1.0 mV s^{-1}. Two main sharp redox peaks can be observed at 0.8–1.0 V and 0.95–0.7 V, respectively, corresponding to multiple redox reactions of V^{5+} in the $VOPO_4 \cdot 2H_2O$ nanosheets (**Figure 2**a). Note that bilayer-VOP nanosheets-based battery exhibits obviously higher response current density with resulted larger specific capacity in CV curve. Apparent difference was also probed in typical galvanostatic charge–discharge (GCD) curve at a current density of 100 mA g^{-1}. As shown in Figure 2b, the bilayer-VOP nanosheets cathode displays a much higher specific capacity of 313.6 mAh g^{-1} with an average discharge plateau of 1.1 V. It is surprising that bilayer-VOP nanosheets cathode delivers a greatly enhanced Zn-ion storage capacity which is about 2.2 times higher than that of bulk-$VOPO_4$ cathode (139.4 mAh g^{-1}). In addition, it possesses superior rate ability with a specific capacity of 313.6, 288.4, 263.3, 234.2, 201.5, and 168.7 mAh g^{-1} at the current of 0.1,

0.5, 1.0, 2.0, 5.0, and 10.0 A g^{-1} respectively, and also a recovered capacity of 292.3 mAh g^{-1} when the current density is set back to 0.1 A g^{-1}. In contrast, the rate capacity of the pristine bulk-$VOPO_4$ is only 139.4, 118.3, 102.1, 79.5, 51.4, 32.7, and 113.8 mAh g^{-1} under the same rate conditions (Figure 2c,d). It is worth noting that the as-observed rate-capability of bilayer-VOP nanosheets exceeds that of recently reported cathode materials in aqueous ZIBs including conventional Mn-based oxides (α-MnO_2,[18] Mn_2O_3,[19] and Mn_3O_4[20]) and V-based compounds ($Na_3V_2(PO_4)_3$,[21] $Zn_3V_2O_7(OH)_2 \cdot 2H_2O$[22]) and Co_3O_4[23] (Figure S3, Supporting Information).

Poor cycling stability is another pivotal issue of layered $VOPO_4 \cdot 2H_2O$ bulk in zinc-ion storage. It is known that $VOPO_4 \cdot 2H_2O$ cathode undergoes severe capacity/voltage fading originated from the decomposition/dissolution of $VOPO_4 \cdot 2H_2O$ in aqueous electrolyte reported recently.6 Such a capacity fading of only 50.7% capacity retention (70.7 mAh g^{-1}) after 500 cycles is also observed in our case for the bulk sample at a current density of 0.1 A g^{-1} (Figure 2e). In contrast, our bilayer-VOP nanosheet cathode displays superior cycling stability with a 94.6% capacity retention (296.8 mAh g^{-1}) after 500 cycles at this low current density. Especially, even cycled at a high current density of 5.0 A g^{-1}, the bilayer-VOP nanosheets cathode likewise deliver a 76.8% retention (158. 5 mAh g^{-1}) after 2, 000 cycles (Figure S4a, Supporting Information). Ex situ XRD patterns clearly reveal the phase evolution of these two cathodes during the long-term charge/discharge cycling. For $VOPO_4 \cdot 2H_2O$ bulk, the layered structure was completely destroyed after 300 cycles at 5 A g^{-1}, which gradually converted into some new phase (Figure S4b, Supporting Information). In contrast, the bilayer bilayer-VOP nanosheets well retained the initial phase structure after this long-term cycling with almost the same X-ray diffraction intensity as the one before cycling. SEM observation confirms the loss of 2D morphology and obvious aggregation after cycling of the bulk sample, while the nanosheet sample can well retain its initial morphology (Figure S4c, Supporting Information). Typical Nyquist plots suggest a higher electrochemical impedance of bulk-$VOPO_4$ cathode when compared with bilayer-VOP nanosheets cathode (Figure S5, Supporting Information). The rapidly increased impedance during the long-term cycle should be mainly ascribed to the incident structure collapse and impurity formation of bulk-$VOPO_4$ cathode, which is demonstrated in Figure 2f,g. All results provide evidence that the electrochemical stability and reversibility is significantly improved in the ultrathin bilayer-VOP nanosheets.

A discharge plateau versus specific capacity diagram for mainstream cathodes of aqueous ZIBs reported in recent years (V-based oxides,[22,24–33] Mn-based compounds,[19,34,35] Prussian Blue analogs,[36–38] polyanion compounds,[10,21,39–42] organics,[43–47] and other chalcogenides[23,48–50]) in **Figure 3**a clearly verifies the merits of our bilayer-VOP nanosheets. Subsequently, its high energy density as well as the power density is also shown in the Ragone plot of Figure 3b. One can see an energy density of 301.4 and 148.7¡$^{-1}$ at a power density of 93.6 and 8798.9 W kg^{-1} can be achieved, respectively, which is one up on numerous vital and hot participants for ZIBs cathode such as $V_3O_7 \cdot nH_2O$,[26] α-MnO_2,[8] $ZnMn_{1.86}O_4$,[34] ZnHCF,[36] and CuHCF.[51]

**ADVANCED
SCIENCE NEWS**

www.advancedsciencenews.com

**ADVANCED
FUNCTIONAL
MATERIALS**

www.afm-journal.de

Figure 2. a) CV curves at the scan rate of 1.0 mV s^{-1}, b) GCD curves at 100 mA g^{-1}, and (c) rate performance of the Zn/ZnSO$_4$/bulk-VOPO$_4$ and Zn/ZnSO$_4$/bilayer-VOP nanosheet ZIBs, respectively. d) GCD curves of Zn/ZnSO$_4$/bilayer-VOP nanosheets battery at different current densities. e) Comparison of the long-term cycle performance at a low current density of 0.1 A g^{-1} of the nanosheet and bulk cathode samples.

In order to figure out the zinc-ion storage mechanism of our bilayer-VOP nanosheets, ex situ XRD characterization was subsequently carried out in a complete discharge–charge cycle (**Figure** 4a). During the discharge process (zinc-ion intercalation), the (001) diffraction peak gradually shifted to higher degree and finally located at 13.5°, corresponding to an interlayer spacing of ≈6.6 Å. When charging to the high voltage (zinc-ion deintercalation), (001) peak shifted back toward lower degree and ultimately located at the similar position compared to that of the initial state (matching with the initial interlayer spacing of ≈7.4 Å, Figure 4b). No impurity diffraction peaks have been detected in all of the XRD results, demonstrating a typical intercalation/deintercalation mechanism for zinc-ion storage in our bilayer-VOP nanosheets. Due to the enhanced electrostatic attraction between intercalated zinc-ion and oxygen in the layers, the interlayer spacing is decreased accompanied with zinc-ion intercalation during the discharge process as reported previously.[5,41] Additionally, the XPS characterization also indicates a reversible

Zn^{2+} intercalation/ deintercalation mechanism in our bilayered ultrathin nanosheets similar with that of bulk VOPO$_4$·2H$_2$O.[5] It is clear the V 2p spectrum *by* ex situ XPS characterization of the initial cathode shows clear characteristic peaks of V^{5+} with a featured binding energy of 518.3 eV, while the appearance of V^{4+} peak at 517.1 eV suggests the existence of [Vo¨]. The V 2p spectrum at the fully discharged state of 0.2 V identifies the disappearance of V^{5+} with emergence of V^{3+} peak at 516.4 eV.[11,13] When charging to the high voltage of 1.9 V, the featured peak of V^{5+} appeared again accompanied with the V^{4+} peak originated from [Vo¨], indicating reversible valence change of V element during the charge/discharge process (Figure 4c). Meanwhile, the Zn 2p spectrum displays prominent peak of Zn at fully discharged state of 0.2 V, corresponding to the zinc-ion intercalation in discharge stage. For the fully charged state at 1.9 V, the intensity of this characteristic signal was significantly decreased (Figure 4d), implying some partial residue of Zn^{2+} after the efficient de-intercalation.[48,49]
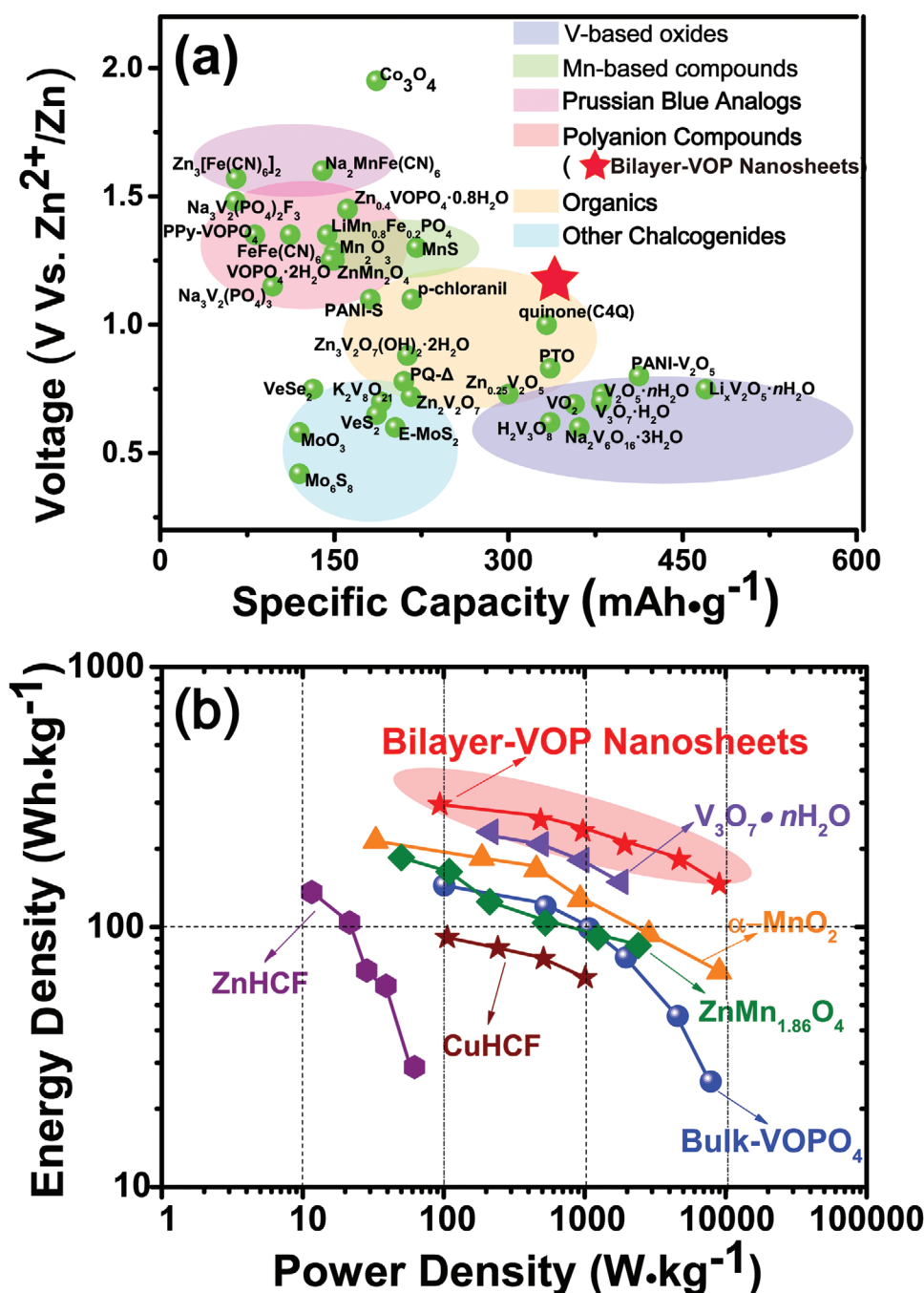
Figure 3. a) Discharge voltage plateau versus specific capacity diagram and b) Ragone plot of bilayer-VOP nanosheets and conventional ZIB cathodes.

2.3. Diffusion Kinetics Analysis

Zinc-ion storage kinetics was then revealed by the galvanostatic intermittent titration technique (GITT) measurement (**Figure 5**a,b). Especially, a drastic increased zinc-ion diffusion coefficient has been detected in bilayer-VOP nanosheets ($\approx 4.6 \times 10^{-7}$ cm^{-2} s^{-1}), which is about 6 orders of magnitude higher than that in bulk-VOPO$_4$ ($\approx 6.1 \times 10^{-13}$ cm^{-2} s^{-1}). Meanwhile, in terms of the CV curves of these two batteries at different scan rate (Figure S6, Supporting Information), dependence of the

logarithm of peak current density and the scan rate is derived. In principle, the peak current (i) and sweep rate (v) in one CV scan follows the rule as the following relationship[52,53]

$$i = av^b \tag{1}$$

where a and b are adjustable values. A b value of 0.5 indicates a semi-infinite diffusion mechanism of the ions, while a b value of 1.0 suggests capacitive behavior. In our case, b value for the predominant peaks of Zn /ZnSO$_4$/ bulk-VOPO$_4$ (peak A, B)
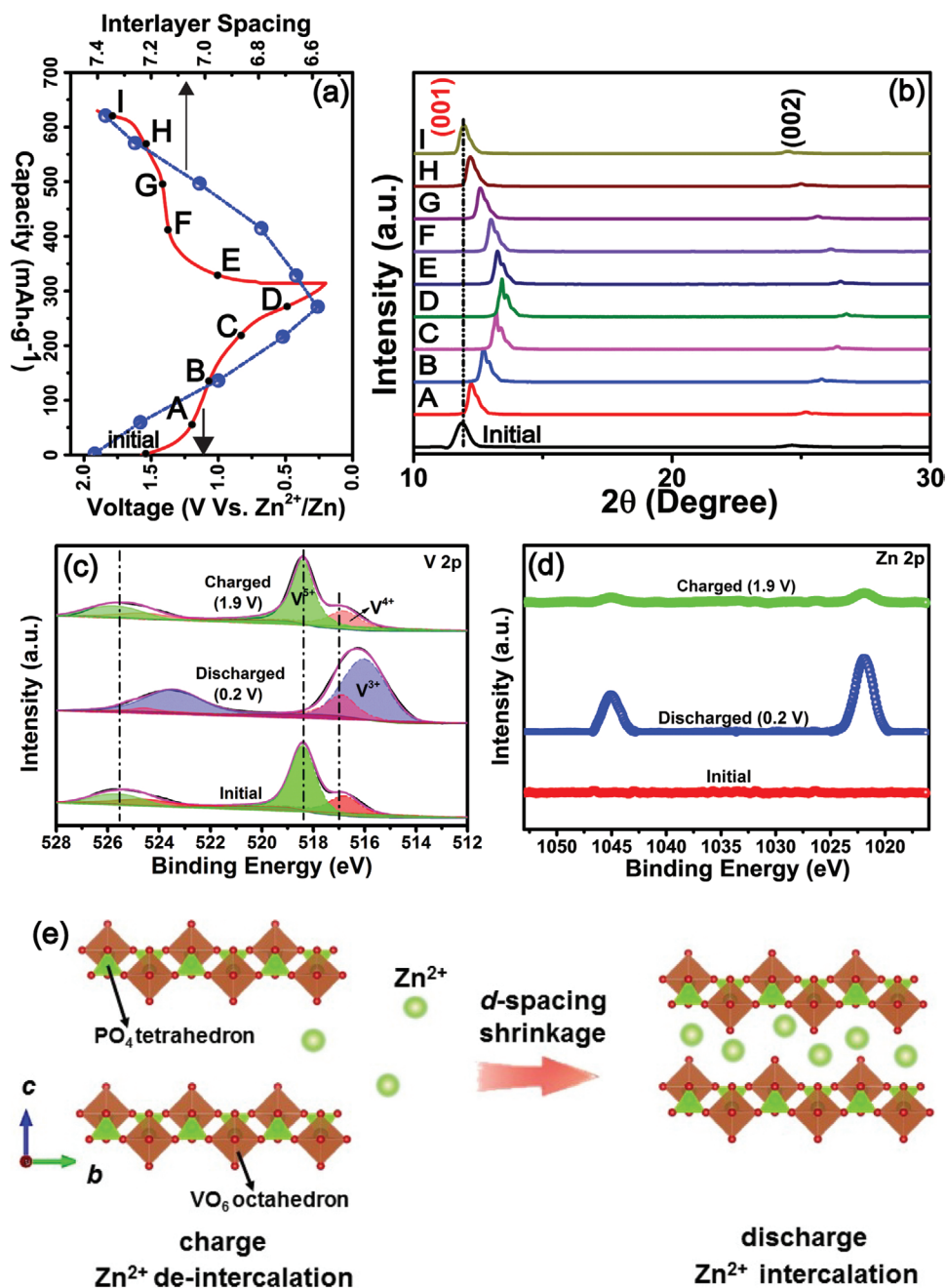
Figure 4. a) GCD curve and the *d*-spacing variation of the bilayer-VOP nanosheets cathode during a complete discharge–charge procedure. b) Corresponding ex situ XRD patterns recorded at different voltage states. c) Ex situ XPS spectrum of V 2p and d) Zn 2p, respectively. e) Schematic illustration of the intercalation/deintercalation mechanism in the bilayer-VOP nanosheets.

are determined to be 0.62, 0.66, whereas the *b* value for corresponding peaks (peaks C and D) in Zn /ZnSO$_4$/ bilayer-VOP nanosheets are calculated to be 0.83 and 0.79, respectively (Figure S7, Supporting Information). Notably, the capacitor-like electrochemical process of (66.2%, 71.8%, 77.6%, 83.1%, and 88.4% at the scan rate of 0.1, 0.2, 0.5, 0.8, and 1.0 mV s^{-1}, respectively) in bilayer-VOP nanosheets cathode is more prominent than that in bulk-VOPO$_4$ cathode (28.4%, 33.2%, 38.9%, 42.8%, and 47.5% at the scan rate of 0.1, 0.2, 0.5, 0.8, and 1.0 mV s^{-1}, respectively) (Figure S8, Supporting Information).

This difference should be attributed to a high specific surface area of 627.3 m^2 g^{-1} of the bilayer-VOP nanosheets compared to that of bulk-VOPO$_4$ (16.8 m^2 g^{-1}).

To deeply clarify the underlying mechanism for the superior electrochemical properties, investigation on structure and electron configuration of the bulk-VOPO$_4$ and bilayer-VOP nanosheets was further conducted. Figure 5c shows the electron paramagnetic resonance (EPR) spectrum of bulk-VOPO$_4$ and bilayer-VOP nanosheets, respectively. Interestingly, the spectrum shows an apparent response signal with a *g* factor
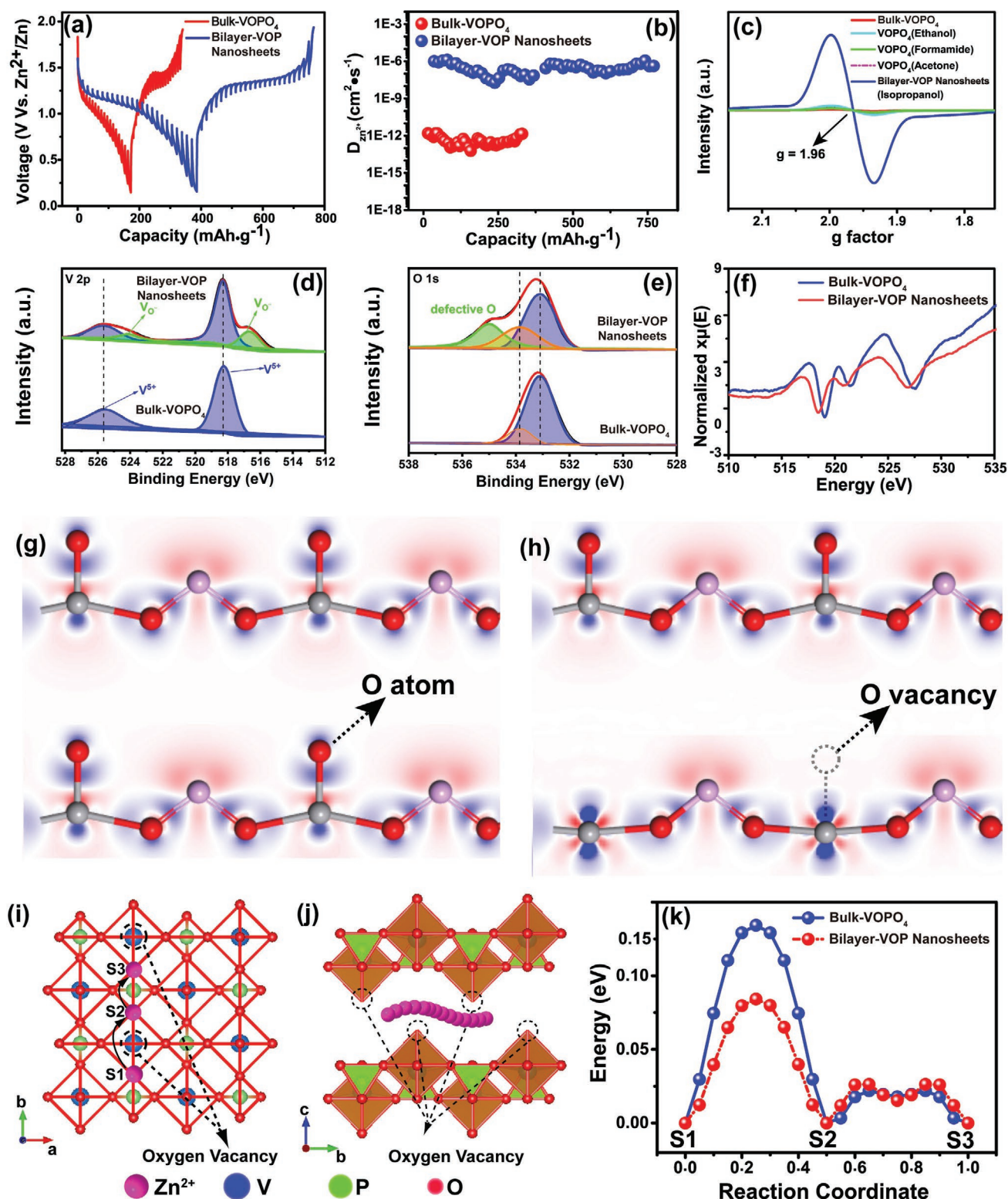
Figure 5. a) GCD curves of the Zn//bulk-VOPO₄ and Zn//bilayer-VOP nanosheets batteries under GITT mode. b) Calculated zinc-ion diffusion coefficient in bulk-VOP and bilayer-VOP nanosheets, respectively. c) EPR spectrum of bulk-VOPO₄, bilayer-VOP nanosheets and VOPO₄·2H₂O treated by ethanol, acetone, and formamide, respectively. d) XPS V 2p and e) O 1s spectrum of bulk-VOPO₄ and bilayer-VOP nanosheets. f) NEXAFS of O K-edge. Schematic illustration of charge distribution for VOPO₄ layers g) without [Vö] and h) after [Vö] introduction. Zn²⁺ diffusion path in [Vö]-rich bilayer-VOP nanosheets along i) [00l] and j) [010] zone axis, respectively. k) Zinc-ion diffusion barrier curve of bulk-VOPO₄ (without [Vö]) and bilayer-VOP nanosheets ([Vö]-rich), respectively.

of 1.96 for bilayer-VOP nanosheets sample, corresponding to paramagnetic tetravalent V^{4+}.[54] However, the signal intensity of bulk-$VOPO_4$ is very weak and almost negligible.[55,56] Considering the high phase purity reflected by XRD patterns of both the two samples, the appearance of V^{4+} indicates the formation of a nonstoichiometric $VOPO_4$ host layer due to the existence of numerous [Vö].[54,57] We found that the [Vö] concentration is highly dependent on the solvent category during the exfoliation process. EPR spectrum of the $VOPO_4 \cdot 2H_2O$ bulk treated by the other solvents (ethanol, acetone, and formamide) using the same exfoliation strategy is also shown in Figure 4c. It is clear the response signals of these three samples are much lower than the one in isopropanol. Since the exfoliation behavior is only observed in isopropanol (Figure 1a), it is rational that the high concentration [Vö] is generally produced during the exfoliation process. Moreover, EPR data for the bilayer-VOP nanosheets cathode after 500 long-term cycles is also shown in Figure S9, Supporting Information. Both of the spectra before and after cycling show an apparent response signal with a *g* factor of 1.96. Although the signal intensity of the sample after 500 cycles is slightly decreased, such a result may provide evidence that [Vö] in bilayer-VOP nanosheets can be well maintained during long-term charge/discharge cycling. We speculate this excellent stability of [Vö] during the charge/discharge process might be ascribed to that zinc-ion intercalation/deintercalation process just occurs in the interlayer spacing rather than the intralayer of the layered framework. Our recent work also clarifies the zinc-ion intercalation/deintercalation occurred in the interlayer spacing of layered $VOPO_4 \cdot 2H_2O$ framework by means of single-crystal XRD (SXRD) characterization via synchrotron and in-plane SAED characterizations.[41] Accordingly, the concentration change of [Vö] in the host layer during the charge/discharge process is very slight and can be neglectful. We further carried out XPS characterization to identify the chemical state change of V element. For V 2p spectrum of bilayer-VOP nanosheets sample (Figure 5d), the characteristic peak located at 518.3 eV in $2p_{3/2}$ region is assigned to V^{5+}, while the nearby split peak at 517.1 eV is the evidence of formation of V^{4+}.[11,41] The same resulted can be also observed from the V $2p_{1/2}$ region. While for bulk-$VOPO_4$ sample, only the characteristic peaks attributed to V^{5+} can be detected. Meanwhile, O 1s spectrum gives a likewise evident proof of [Vö] formation in the exfoliated sample (Figure 5e). In addition to the characteristic peak at 533.2 and 533.9 eV ascribed to intrinsic lattice O in $VOPO_4$ framework, respectively, an extra peak is detected at ≈535 eV for bilayer-VOP nanosheets sample, which is attributed to the defective oxygen.[58] No obvious difference has been identified from the P 2p spectrum of these two sample, manifesting the stability of [PO_4] tetrahedron together with unchanged valence of P element during the liquid-exfoliation (Figure S10, Supporting Information). In this regard, it is rational that the abundant [Vö] is stabilized in the corner of [VO_6] octahedron rather than the [PO_4] tetrahedron. Moreover, an X-ray absorption near edge structure (XANES) profile for O element of bulk-$VOPO_4$ and bilayer-VOP nanosheets is shown in Figure 5f, respectively. Apparently, the normalized absorption curve of bilayer-VOP nanosheets sample shows much decreased intensity with broadening peak feature in contrast

with the bulk-$VOPO_4$. Such a result is similar with that reported by Lu and co-workers and Wang and co-workers,[58,59] and also provides direct evidence for the formation of [Vö] in the bilayer nanosheets.

DFT simulation is then employed for visually identifying the change of electron structure with [Vö] introduction. The noteworthy negative charge distribution (red region) around O atom is thereupon observably centralized to V atom when [Vö] is introduced in the [VO_6] unit (Figure 5g,h). The negative charge center is thus overall shifted toward the $VOPO_4$ layers and far away from the interlayer transport channel, hence the powerful electrostatic interaction between zinc-ion and $VOPO_4$ layers will be permanently released for superior diffusion kinetics. A Climbing-image nudged elastic band (CI-NEB) method is performed for better understanding how [Vö] plays a decisive role in the improvement of Zn^{2+} diffusion kinetics and storage capacity. As shown in Figure 5i,j, a preferred site for Zn^{2+} absorption is determined on the top site of the corner-shared oxygen atom of [PO_4] tetrahedron and [VO_6] octahedron, while the optimized transport path for Zn^{2+} is from the top site of the first corner-shared O atom (S1), via the adjacent corner-shared O atom (S2), to the next periodic corner-shared O atom site (S3). Clearly, the introduction of O vacancy in [VO_6] octahedron will not change the preferred absorption site and transport path. However, the energy barrier is much reduced especially when Zn^{2+} migrating through the top site of [VO_6]. Similar zinc-ion transport path is also simulated in the interlayer spacing of [Vö] poor framework with more distinct movement along *c* axis due to the stronger electrostatic interaction between zinc-ion and the lattice oxygen in [VO_6] (Figure S11, Supporting Information). The energy barrier of a complete diffusion process shows a drastic decrease from 0.13 to 0.08 eV of bulk-$VOPO_4$ and bilayer-VOP nanosheets, respectively (Figure 5k). Accordingly, the Zn^{2+} diffusion kinetics can be significantly improved due to such a drastically decreased energy barrier (≈0.08 eV) in [Vö]-rich bilayer-VOP nanosheets.

The successful introduction of [Vö] also results in an improvement of electron conductivity confirmed by a Mott–Schottky (impedance-potential) measurement. The positive slope of Mott–Schottky plots demonstrate n-type semiconductor property of both samples (Figure S12, Supporting Information). In accordance to the inverse proportion between carrier concentration and the slope,[58,60] an ≈57-fold increased carrier concentration of bilayer-VOP nanosheets can be obtained compared to the precursor bulk-$VOPO_4$. Such a result is well in consistent with the bandgap decrease from the corresponding DFT simulation in Figure 1c. The as-observed enhanced conductivity and boosting zinc-ion transport by a smaller energy barrier should be the origin of the superior battery performance on specific capacity, energy density, rate-capability and long-term cyclability. In addition, rich oxygen vacancies in our bilayered nanosheets are favorable to suppress the needless phase transition of the electrode so as to well stabilize the phase structure during the long-term charge/discharge process.[61–63] Especially, further study on the facile preparation and electrochemical investigation of [Vö]-rich $VOPO_4 \cdot 2H_2O$ bulk may be also interesting and valuable to see if any changes can be observed without its ultrathin feature.
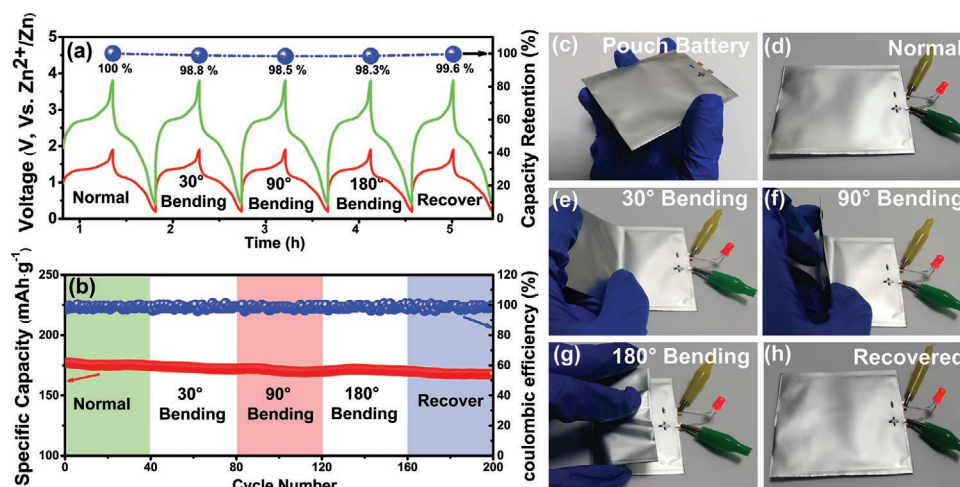
Figure 6. a) GCD curves of a Zn//bilayer-VOP nanosheets pouch battery and two batteries in series under various bending state (normal, 30°, 90°, 180°, and recovered), respectively. b) Lifespan test of the pouch battery at 1.0 A g^{-1} under various bending states. c) Soft-packed Zn//bilayer-VOP nanosheets battery and d–h) LED driving test under varied bending state, respectively.

2.4. Application Potential for Flexible Battery

To further verify the practical application in flexible and wearable device, soft-packed battery pouch based on slurry-coated bilayer-VOP nanosheets @ carbon fiber cloth (CFC) flexible cathode, 1 M Zn(ClO$_4$)$_2$ @ polyvinyl alcohol (PVA) electrolyte and electrodeposited Zn @ CFC anodes were assembled successfully. ZnSO$_4$ electrolyte was replaced by Zn(ClO$_4$)$_2$ here because of the higher solubility of Zn(ClO$_4$)$_2$ in PVA aqueous solution.[41] SEM image of a CFC-based Zn electrodeposited anode reflects the well-covered surface with Zn thin layer (Figure S13, Supporting Information). A continuous GCD test of an assembled pouch battery as well as two batteries in series under different bending states (0°, 30°, 90°, 180°, and recovered) shows stable charge–discharge curve (**Figure 6**a), respectively, implying its satisfied flexibility and folding ability. Further cyclic charge–discharge test at 1.0 A g^{-1} also confirms its long lifespan with reliable flexibility (94.4% capacity retention in 200 cycles) (Figure 6b). Furthermore, the well-packaged pouch battery could likewise drive a red light emitting diode (LED) steadily under the varied bending state in fully charged status (Figure 6c–h).

3. Conclusions

In summary, we realized a large scale produce of [Vo¨]-rich bilayer bilayer-VOP nanosheets via a facile liquid exfoliation strategy. The high-concentration of [Vo¨] was carefully confirmed by XPS, EPR, and XANES characterizations. As the cathode of aqueous ZIB, the bilayer-VOP nanosheets exhibits much improved specific capacity (313.6 mAh g^{-1} at 0.1 A g^{-1}), rate capability (168.7 mAh g^{-1} at 10 A g^{-1}) and long-term stability. Compared with the sluggish diffusion kinetics in bulk-VOPO$_4$ with a low coefficient of 6.1×10^{-13} cm^2 s^{-1}, almost 6 orders of magnitude higher diffusion coefficient have been found in the bilayer-VOP nanosheets (4.6×10^{-7} cm^{-2} s^{-1}). DFT simulation identifies the barrier energy for zinc-ion diffusion is also remarkably decreased from 1.3 to 0.08 eV after the introduction of high

concentration [Vo¨]. Mott–Schottky (impedance-potential) measurement also demonstrates a great increase on electronic conductivity with ≈57-fold increased carrier concentration owing to its high-concentration [Vo¨]. Our study provides a novel 2D bilayer-VOP nanosheets to boost zinc-ion transport properties by introducing high-concentration oxygen vacancies. Owing to their outstanding electrochemical performance, safety and flexibility, these 2D bilayer-VOP nanosheets may hold promise in the next-generation energy storage devices.

4. Experimental Section

Synthesis of VOPO$_4$·2H$_2$O Bulk (Bulk-VOPO$_4$) and Fabrication of Bilayer VOPO$_4$ Nanosheets (Bilayer-VOP Nanosheets): The precursor bulk-VOPO$_4$ is synthesized based on a convenient oil bath refluxing method reported in the early literature. In a typical procedure, 4.8 g of V$_2$O$_5$, 26.6 mL of H$_3$PO$_4$, and 115.4 mL DI water were added into a three-necked flask, followed by a short-time magnetic stirring and then heated at 110 °C in the oil bath with reflux condensation. After the reaction system was cooling down to the room temperature naturally, the yellow precipitate was collected by centrifugation wash of DI water and acetone for 3 times, respectively. The resulting sample was dried at 60 °C in the vacuum oven so as to obtain bulk-VOPO$_4$. bilayer-VOP nanosheets is obtained by dispersing certain amount of bulk-VOPO$_4$ (0.5 g) into the isopropanol solvent (50 mL) and followed by a continuous stirring for 24 h. The finally formed transparent colloidal solution was centrifuged at 8000 rpm for 10 min to obtain the bilayer-VOP nanosheets at the bottom of tube, which can be collected and dried in an oven at 60 °C for further study.

Material Characterization: The structure morphology and structure characterization were characterized by scanning electron microscopy (SEM, Phenom Pro X), high-resolution transmission electron microscopy (TEM) and X-ray diffraction (XRD, Bruker D8-A25 diffractometer using Cu Kα radiation (λ = 1.5406 Å)). The selected electron diffraction (SAED) and energy-dispersive spectrum (EDS-mapping) were carried out during the TEM measurement (Philips CM 200 FEG Field Emission Microscope) process to gather detailed information of phase structure and chemical element distribution of the sample. Further information of the chemical bonding condition was recorded by means of X-ray photoelectron spectrum (XPS, PHI 5000C EACA), Raman spectrum (RENISHAW inVia), Fourier transform infrared spectroscopy (FTIR, BRUKER TENSOR II) and electron paramagnetic resonance (EPR, Bruker

A300 spectrometer), respectively. The X-ray absorption spectra were collected on the beamline BL20A1 in NSRRC, and technically supported by Ceshigo Research Service. The radiation was monochromatized by a Si (111) double-crystal monochromator. XANES and EXAFS data reduction and analysis were processed by Athena software. Specific surface area was performed using Brunner-Emmet–Teller method (Quadrasorb evo).

Electrochemical Measurement: Bulk-VOPO$_4$ and bilayer-VOP nanosheets cathode for aqueous ZIBs was prepared by mixing as-prepared sample, acetylene black and polyvinylidene fluoride as (PVDF) on the basis of a mass ratio of 7:2:1 with the moderate addition of 1-methyl-2-pyrrolidinone (NMP), respectively. Then, the uniform slurry was coated onto a piece of 304 stainless-steel foil and drying at 110 °C for 12 h in a vacuum oven. The slurry-coated foil was cut into Φ15 mm electrodes served as the cathode, while the zinc foil washed with ethanol and glass fiber membrane were used as the anode and separator, respectively, and 2 M ZnSO$_4$ was prepared as the electrolyte. The mass loading of the coated slurry on the substrate is ≈2 mg cm^{-2} on average. The CR-2032 cell was assembled in air using the beforehand electrodes and other relevant components. LAND battery test system (CT2001A) was employed to evaluate the electrochemical performance of the battery, including galvanostatic charge–discharge (GCD), rate capability and long-term cycle performance. Cyclic voltammetry (CV) test at different scan rate and Mott–Schottky plot (impedance-potential test) under a frequency of 1 kHz is performed on the electrochemical workstation (CHI660E), respectively.

Fabrication of the Pouch Battery: The pouch battery was fabricated using aforementioned slurry-coated carbon fiber cloth (CFC) as the cathode (mass loading: 2 mg cm^{-2}), CFC with a layer of zinc electrodeposited coating as the anode, a piece of filter paper as the separator and 2 M Zn(ClO$_4$)$_2$ @polyvinyl alcohol (PVA) as the electrolyte. The electrolyte was prepared by adding 3 g of PVA to 30 mL of 2 M Zn(ClO$_4$)$_2$ aqueous solution little by little with continuous stirring, followed by oil bath treatment at 80 °C for 2h and gathering the gel-like sample when the system is cooled down to the room temperature. The electrochemical deposition of zinc layer on the CFC was carried out on CHI660E using potentiostatic model at −0.7 V (vs Zn^{2+}/Zn) for 2000 s. The fully assembled pouch battery was finally sealed with aluminum foil as a sandwich structure.

Calculation Methods: The calculation method for the capacity contribution is based on the following equation

$$I_p = C_1 \nu + C_2 \nu^{\frac{1}{2}} \tag{2}$$

where I_p (A g^{-1}) is the peak current density at different scan rate, ν (mV s^{-1}) is the specific scan rate, and C1 and C2 are the corresponding constant factors of the capacity contribution of surface pseudocapacitive effect and battery-type effect, respectively.

With a deformation of the above equation, the specific contribution rate of different internal mechanisms can be solved according to the following equation

$$\frac{I_p}{\nu^{\frac{1}{2}}} = C_1 \nu^{\frac{1}{2}} + C_2 \tag{3}$$

The specific energy density (Wh kg^{-1}) and average specific power density (W kg^{-1}) of the Zn/VSe2 batteries were calculated in terms of the following equations:

$$E_s = \int_{V_0}^{V_1} C_s(V) \tag{4}$$

$$P_s = \frac{E_s}{t} \tag{5}$$

where E_s is the calculated specific energy density (Wh kg^{-1}), P_s is the average specific power density (W kg^{-1}), C_s (mAh g^{-1}) is the specific capacity of the battery, V_0 and V_1 are the voltage lower limit and voltage

upper limit of discharge procedure, respectively, and t is the discharge time (h).

Diffusion coefficient of zinc-ion (D_{Zn}^{2+}) can be experimentally calculated by GITT method in terms of the following equation

$$D = \frac{4}{\pi \tau} \left(\frac{n_m V_m}{S} \right)^2 \left(\frac{\Delta E_s}{\Delta E_t} \right)^2 \tag{6}$$

where D is the diffusion coefficient of zinc ion, τ is the relaxation time of current pulse, n_m, V_m, and S are the corresponding mole number, mole volume, and the exposed surface area of active material, severally; ΔE_s and ΔE_t are the voltage change produced by current pulse and the galvanostatic charge/discharge, respectively.

Simulation Details: The modeling in this study was performed in the framework of the DFT as implemented in the Vienna Ab initio Simulation Package (VASP). The functional of Perdew–Burke–Ernzerhof based on generalized gradient approximation (GGA) was applied to describe the exchange-correlation energy. In addition, the zero damping DFT-D3 dispersion correction method of Grimme was accounted for VdW interaction in the system. A vacuum space of 15 Å was adopted. The plane-wave cutoff energy was set to be 480 eV, and the k-mesh was determined to be $7 \times 7 \times 1$ according to the convergence test, which makes the energy accuracy within 1.0×10^{-3} eV atom^{-1}. Finally, a double-layered VOPO$_4$ model was constructed, with the corresponding interlayer spacing obtained from the previous XRD and HRTEM analysis, thereby the diffusion of zinc ion between VOPO$_4$ layers was simulated using the climbing-image nudged elastic band method.

Supporting Information

Supporting Information is available from the Wiley Online Library or from the author.

Acknowledgements

Conflict of Interest

The authors declare no conflict of interest.

Data Availability Statement

Research data are not shared.

Keywords

**ADVANCED
SCIENCE NEWS**

www.advancedsciencenews.com

**ADVANCED
FUNCTIONAL
MATERIALS**

www.afm-journal.de

[1] M. Chhowalla, H. S. Shin, G. Eda, L. J. Li, K. P. Loh, H. Zhang, *Nat. Chem.* **2013**, *5*, 263.

[2] Q. B. Yun, L. X. Li, Z. N. Hu, Q. P. Lu, B. Chen, H. Zhang, *Adv. Mater.* **2020**, *32*, 1903826.

[3] C. Z. Wu, X. L. Lu, L. L. Peng, K. Xu, X. Peng, J. L. Huang, G. H. Yu, Y. Xie, *Nat. Commun.* **2013**, *4*, 2431.

[4] N. G. Park, K. M. Kim, S. H. Chang, *Electrochem. Commun.* **2001**, *3*, 553.

[5] F. Wan, Y. Zhang, L. L. Zhang, D. B. Liu, C. D. Wang, L. Song, Z. Q. Niu, J. Chen, *Angew. Chem., Int. Ed.* **2019**, *58*, 7062.

[6] H. Y. Shi, Y. Song, Z. M. Qin, C. C. Li, D. Guo, X. X. Liu, X. Q. Sun, *Angew. Chem., Int. Ed.* **2019**, *58*, 16057.

[7] P. Canepa, G. S. Gautam, D. C. Hannah, R. Malik, M. Liu, K. G. Gallagher, K. A. Persson, G. Ceder, *Chem. Rev.* **2017**, *117*, 4287.

[8] C. J. Xu, B. H. Li, H. D. Du, F. Y. Kang, *Angew. Chem., Int. Ed.* **2012**, *51*, 933.

[9] G. Z. Fang, J. Zhou, A. Q. Pan, S. Q. Liang, *ACS Energy Lett.* **2018**, *3*, 2480.

[10] F. Wang, W. Sun, Z. Shadike, E. Y. Hu, X. Ji, T. Gao, X. Q. Yang, K. Xu, C. S. Wang, *Angew. Chem., Int. Ed.* **2018**, *57*, 11978.

[11] N. F. Quackenbush, L. Wangoh, D. O. Scanlon, R. Zhang, Y. Chung, Z. Chen, B. Wen, Y. Lin, J. C. Woicik, N. A. Chernova, S. P. Ong, M. S. Whittingham, L. F. J. Piper, *Chem. Mater.* **2015**, *27*, 8211.

[12] Y. N. Song, P. Y. Zavalij, M. S. Whittingham, *J. Electrochem. Soc.* **2005**, *152*, A721.

[13] Y. X. Zeng, Z. Z. Lai, Y. Han, H. Z. Zhang, S. L. Xie, X. H. Lu, *Adv. Mater.* **2018**, *30*, 1802396.

[14] N. Yamamoto, N. Hiyoshi, T. Okuhara, *Chem. Mater.* **2002**, *14*, 3882.

[15] B. Yan, L. Liao, Y. M. You, X. J. Xu, Z. Zheng, Z. X. Shen, J. Ma, L. M. Tong, T. Yu, *Adv. Mater.* **2009**, *21*, 2436.

[16] L. Benes, K. Melanova, M. Trchova, P. Capkova, P. Matejka, *Eur. J. Inorg. Chem.* **1999**, *12*, 2289.

[17] Y. C. Huang, B. Long, M. N. Tang, Z. B. Rui, M. S. Balogun, Y. X. Tong, H. B. Ji, *Appl. Catal., B* **2016**, *181*, 779.

[18] W. Sun, F. Wang, S. Y. Hou, C. Y. Yang, X. L. Fan, Z. H. Ma, T. Gao, F. D. Han, R. Z. Hu, M. Zhu, C. S. Wang, *J. Am. Chem. Soc.* **2017**, *139*, 9775.

[19] B. Z. Jiang, C. J. Xu, C. L. Wu, L. B. Dong, J. Li, F. Y. Kang, *Electrochim. Acta* **2017**, *229*, 422.

[20] C. Y. Zhu, G. Z. Fang, J. Zhou, J. H. Guo, Z. Q. Wang, C. Wang, J. Y. Li, Y. Tang, S. Q. Liang, *J. Mater. Chem. A* **2018**, *6*, 9677.

[21] G. L. Li, Z. Yang, Y. Jiang, C. H. Jin, W. Huang, X. L. Ding, Y. H. Huang, *Nano Energy* **2016**, *25*, 211.

[22] C. Xia, J. Guo, Y. J. Lei, H. F. Liang, C. Zhao, H. N. Alshareef, *Adv. Mater.* **2018**, *30*, 1705580.

[23] L. T. Ma, S. M. Chen, H. F. Li, Z. H. Ruan, Z. J. Tang, Z. X. Liu, Z. F. Wang, Y. Huang, Z. X. Pei, J. A. Zapien, C. Y. Zhi, *Energy Environ. Sci.* **2018**, *11*, 2521.

[24] J. W. Ding, Z. G. Du, L. Q. Gu, B. Li, L. Z. Wang, S. W. Wang, Y. J. Gong, S. B. Yang, *Adv. Mater.* **2018**, *30*, 1800762.

[25] M. Y. Yan, P. He, Y. Chen, S. Y. Wang, Q. L. Wei, K. N. Zhao, X. Xu, Q. Y. An, Y. Shuang, Y. Y. Shao, K. T. Mueller, L. Q. Mai, J. Liu, J. H. Yang, *Adv. Mater.* **2018**, *30*, 1703725.

[26] D. Kundu, S. H. Vajargah, L. W. Wan, B. Adams, D. Prendergast, L. F. Nazar, *Energy Environ. Sci.* **2018**, *11*, 881.

[27] Q. Pang, C. L. Sun, Y. H. Yu, K. N. Zhao, Z. Y. Zhang, P. M. Voyles, G. Chen, Y. J. Wei, X. D. Wang, *Adv. Energy Mater.* **2018**, *8*, 1800144.

[28] V. Soundharrajan, B. Sambandam, S. Kim, M. H. Alfaruqi, D. Y. Putro, J. Jo, S. Kim, V. Mathew, Y. K. Sun, J. Kim, *Nano Lett.* **2018**, *18*, 2402.

[29] D. Kundu, B. D. Adams, V. Duffort, S. H. Vajargah, L. F. Nazar, *Nat. Energy* **2016**, *1*, 16119.

[30] B. Y. Tang, G. Z. Fang, J. Zhou, L. B. Wang, Y. P. Lei, C. Wang, T. Q. Lin, Y. Tang, S. Q. Liang, *Nano Energy* **2018**, *51*, 579.

[31] B. Sambandam, V. Soundharrajan, S. Kim, M. H. Alfaruqi, J. Jo, S. Kim, V. Mathew, Y. K. Sun, J. Kim, *J. Mater. Chem. A* **2018**, *6*, 3850.

[32] Y. Q. Yang, Y. Tang, G. Z. Fang, L. T. Shan, J. S. Guo, W. Y. Zhang, C. Wang, L. B. Wang, J. Zhou, S. Q. Liang, *Energy Environ. Sci.* **2018**, *11*, 3157.

[33] S. C. Liu, H. Zhu, B. H. Zhang, G. Li, H. K. Zhu, Y. Ren, H. B. Geng, Y. Yang, Q. Liu, C. C. Li, *Adv. Mater.* **2020**, *32*, 200113.

[34] N. Zhang, F. Y. Cheng, Y. C. Liu, Q. Zhao, K. X. Lei, C. C. Chen, X. S. Liu, J. Chen, *J. Am. Chem. Soc.* **2016**, *138*, 12894.

[35] W. B. Liu, J. W. Hao, C. J. Xu, J. Mou, L. B. Dong, F. Y. Jiang, Z. Kang, J. L. Wu, B. Z. Jiang, F. Y. Kang, *Chem. Commun.* **2017**, *53*, 6872.

[36] L. Y. Zhang, L. Chen, X. F. Zhou, Z. P. Liu, *Adv. Energy Mater.* **2015**, *5*, 1400930.

[37] Z. Liu, G. Pulletikurthi, F. Endres, *ACS Appl. Mater. Interfaces* **2016**, *8*, 12158.

[38] Z. G. Hou, X. Q. Zhang, X. N. Li, Y. C. Zhu, J. W. Liang, Y. T. Qian, *J. Mater. Chem. A* **2017**, *5*, 730.

[39] W. Li, K. L. Wang, S. J. Cheng, K. Jiang, *Energy Storage Mater.* **2018**, *15*, 14.

[40] J. W. Zhao, Y. Q. Li, X. Peng, S. M. Dong, J. Ma, G. L. Cui, L. Q. Chen, *Electrochem. Commun.* **2016**, *69*, 6.

[41] Z. Y. Wu, Y. N. Wang, L. Zhang, L. Jiang, W. C. Tian, C. L. Cai, J. Price, Q. F. Gu, L. F. Hu, *ACS Appl. Energy Mater.* **2020**, *3*, 3919.

[42] V. Verma, S. Kumar, W. Manalastas, J. Zhao, R. Chila, S. Z. Meng, P. Kidkhunthod, M. Srinivasan, *ACS Appl. Energy Mater.* **2019**, *2*, 8667.

[43] Q. Zhao, W. W. Huang, Z. Q. Luo, L. J. Liu, Y. Lu, Y. X. Li, L. Li, J. Y. Hu, H. Ma, J. Chen, *Sci. Adv.* **2018**, *4*, eaao1761.

[44] D. Kundu, P. Oberholzer, C. Glaros, A. Bouzid, E. Tervoort, A. Pasquarello, M. Niederberger, *Chem. Mater.* **2018**, *30*, 3874.

[45] K. W. Nam, H. Kim, Y. Beldjoudi, T. W. Kwon, D. J. Kim, J. F. Stoddart, *J. Am. Chem. Soc.* **2020**, *142*, 2541.

[46] Z. W. Guo, Z. Y. Ma, X. L. Dong, J. H. Huang, Y. G. Wang, Y. Y. Xia, *Angew. Chem., Int. Ed.* **2018**, *57*, 11737.

[47] H. Y. Shi, Y. J. Ye, K. Liu, Y. Song, X. Q. Sun, *Angew. Chem., Int. Ed.* **2018**, *57*, 16359.

[48] Z. Y. Wu, C. J. Lu, Y. N. Wang, L. Zhang, L. Jiang, W. C. Tian, C. L. Cai, Q. F. Gu, Z. M. Sun, L. F. Hu, *Small* **2020**, *16*, 2000698.

[49] P. He, M. Y. Yan, G. B. Zhang, R. M. Sun, L. N. Chen, Q. Y. An, L. Q. Mai, *Adv. Energy Mater.* **2017**, *7*, 1601920.

[50] H. F. Li, Q. Yang, F. N. Mo, G. J. Liang, Z. X. Liu, Z. J. Tang, L. T. Ma, J. Liu, Z. C. Shi, C. Y. Zhi, *Energy Storage Mater.* **2019**, *19*, 94.

[51] R. Trocoli, F. L.a Mantia, *ChemSusChem* **2015**, *8*, 481.

[52] Y. Yan, B. Hao, D. Wang, G. Chen, E. Markweg, A. Albrecht, P. Schaaf, *J. Mater. Chem. A* **2013**, *1*, 14507.

[53] Y. Gogotsi, R. M. Penner, *ACS Nano* **2018**, *12*, 2081.

[54] J. Krzystek, A. Ozarowski, J. Telser, D. C. Crans, *Coord. Chem. Rev.* **2015**, *301*, 123.

[55] Q. S. Wang, Y. F. Zhang, J. Q. Zheng, T. Hu, C. G. Meng, *Microporous Mesoporous Mater.* **2017**, *244*, 264.

[56] A. Adamski, T. Spalek, Z. Sojka, *Res. Chem. Intermed.* **2003**, *29*, 793.

[57] M. Occhiuzzi, D. Cordischi, R. Dragone, *J. Solid State Chem.* **2005**, *178*, 1551.

[58] H. Z. Zhang, J. Wang, Q. Y. Liu, W. Y. He, Z. Z. Lai, X. Y. Zhang, M. H. Yu, Y. X. Tong, X. H. Lu, *Energy Storage Mater.* **2019**, *21*, 154.

[59] Y. Zhang, Y. X. Hu, Z. L. Wang, T. G. Lin, X. B. Zhu, B. Luo, H. Hu, W. Xing, Z. F. Yan, L. Z. Wang, *Adv. Funct. Mater.* **2020**, *30*, 2004172.

[60] X. H. Lu, G. M. Wang, T. Zhai, M. H. Yu, J. Y. Gan, Y. X. Tong, Y. Li, *Nano Lett.* **2012**, *12*, 1690.

[61] Z. Q. Li, Y. K. Ren, L. Mo, C. F. Liu, K. Hsu, Y. C. Ding, X. X. Zhang, X. Li, L. H. Hu, D. H. Ji, G. Z. Cao, *ACS Nano* **2020**, *14*, 5581.

[62] H. S. Kim, J. B. Cook, H. Lin, J. S. Ko, S. H. Tolbert, V. Ozolins, B. Dunn, *Nat. Mater.* **2017**, *16*, 454.

[63] T. Xiong, Z. G. Yu, H. J. Wu, Y. Du, Q. D. Xie, J. S. Chen, Y. W. Zhang, S. J. Pennycook, W. S. V. Lee, J. M. Xue, *Adv. Energy Mater.* **2019**, *9*, 1803815.